Atmos. Chem. Phys. Discuss., 8, 15901–15939, 2008
www.atmos-chem-phys-discuss.net/8/15901/2008/

Atmospheric Chemistry and Physics Discussions

This discussion paper is/has been under review for the journal *Atmospheric Chemistry and Physics (ACP)*. Please refer to the corresponding final paper in *ACP* if available.

Cloud phase identification of low-level Arctic clouds from airborne spectral radiation measurements: test of three approaches

A. Ehrlich[1], E. Bierwirth[1], M. Wendisch[1], J.-F. Gayet[2], G. Mioche[2], A. Lampert[3], and J. Heintzenberg[4]

[1]Johannes Gutenberg-University Mainz, Institute for Atmospheric Physics, Mainz, Germany
[2]Laboratoire de Météorologie Physique (LAMP), Univ. Blaise Pascal, Aubière Cedex, France
[3]Alfred Wegener Institute for Polar and Marine Research, Potsdam, Germany
[4]Leibniz-Institute for Tropospheric Research, Leipzig, Germany

Received: 22 July 2008 – Accepted: 22 July 2008 – Published: 20 August 2008

Correspondence to: A. Ehrlich (ehrlicha@uni-mainz.de)

Published by Copernicus Publications on behalf of the European Geosciences Union.

Abstract

Boundary layer clouds were investigated with a complementary set of remote sensing and in situ instruments during the Arctic Study of Tropospheric Aerosol, Clouds and Radiation (ASTAR) campaign in March and April 2007. The clouds that formed in a cold air outbreak over the open Greenland sea showed a variety in their thermodynamic state. Beside the predominant mixed-phase clouds pure liquid and ice clouds were observed. Utilizing the measurements of solar radiation reflected by the clouds three methods to retrieve the thermodynamic phase of the cloud were defined and compared. Two ice indices I_S and I_P were obtained by analyzing the spectral pattern of the cloud top reflectance in the near infrared (1500–1800 nm wavelength) characterized by ice and water absorption. A third ice index I_A is based on the different side scattering of spherical liquid water particles and nonspherical ice crystals which was recorded in simultaneous measurements of cloud albedo and reflectance.

Radiative transfer simulations showed that I_S, I_P and I_A range between 5 to 80, 0 to 20 and 1 to 1.25, respectively, with lowest values indicating pure liquid water clouds and highest values pure ice clouds. I_S and I_P were found to be strongly sensitive to the effective diameter of the ice crystals present in the cloud. Therefore the identification of mixed-phase clouds requires a priori knowledge of the ice crystal dimension. I_A has the disadvantage that this index is mainly dominated by the uppermost cloud layer ($\tau<1.5$). Typical boundary layer mixed-phase clouds with a liquid cloud top layer will be identified as pure liquid water clouds. All three methods were applied to measurements above a cloud field observed during ASTAR 2007. The comparison with independent in situ microphysical measurements showed a good agreement in identifying the dominant mixed-phase clouds and a pure ice cloud at the edge of the cloud field.

1 Introduction

The impact of clouds on the radiation budget of Arctic regions constitutes a crucial uncertainty in predicting Arctic climate change as reported in the Arctic Climate Impact Assessment (Corell, 2004). Mostly Arctic clouds are warming the underlying atmosphere (Intrieri et al., 2002). Due to the high albedo of the snow or ice-covered surfaces the longwave radiative heating dominates over the solar cooling and thus determines the cloud radiative forcing in the Arctic. Shupe and Intrieri (2004) showed that low-level clouds are the most important contributors to the Arctic surface radiation budget. Their radiative impact is highly variable and depends on surface albedo, aerosol particles, cloud water content, cloud particle size and cloud thermodynamic phase (Curry et al., 1996; Shupe and Intrieri, 2004).

For instance, a low surface albedo in summer leads to a seasonal cooling effect due to Arctic clouds (Dong and Mace, 2003). Freese and Kottmeier (1998) showed for marine clouds that the low surface albedo of the ice free ocean reduces the upwelling radiation above the overlaying clouds and thus the cloud albedo by up to 30% compared to clouds over highly reflecting sea ice. Cloud radiative properties and cloud life cycle are also influenced by the cloud thermodynamic phase (Sun and Shine, 1994; Harrington et al., 1999; Yoshida and Asano, 2005; Ehrlich et al., 2008b). The simulations by Harrington et al. (1999) showed that the cloud top temperature and the amount of ice nuclei control the conversion of liquid cloud water to solid ice. Cold temperatures and high ice nuclei concentrations lead to higher ice fractions and shorten the life time of the mixed-phase cloud. Furthermore, Yoshida and Asano (2005) showed that an increasing ice fraction results in a significant increase in the absorptance of mixed-phase clouds for the near infrared wavelength range (>700 nm).

Therefore, in situ measurements and/or remote sensing of the thermodynamic cloud phase are of importance. Parameterizations of the dependence of ice volume fraction (ratio of ice to total water content) and cloud temperature were obtained from in situ measurements by Boudala et al. (2004); Korolev et al. (2003). However, due to the

ACPD
8, 15901–15939, 2008

Title Page
Abstract Introduction
Conclusions References
Tables Figures
◀◀ ▶▶
◀ ▶
Back Close
Full Screen / Esc
Printer-friendly Version
Interactive Discussion

limitation in time and space in situ measurements can give a snapshot of the complexity of Arctic clouds only (Lawson et al., 2001; Cober et al., 2001; McFarquhar et al., 2007).

Several cloud retrieval algorithms based on satellite data provide the cloud phase. Commonly, before retrieving cloud properties a preselection algorithm distinguishes between ice, mixed-phase and liquid water clouds (Key and Intrieri, 2000; King et al., 2004; Kokhanovsky et al., 2006). This phase discrimination is often based on two methods using the brightness temperatures of thermal infrared (IR; 5–50 μm) channels and the cloud reflectance at channels for solar radiation in the visible (VIS; 300–700 nm) and near infrared wavelength range (NIR; >700 nm). Further methods are based on radar data (CloudSat, Sassen and Wang, 2008) and polarization measurements, for example using data of the POLarization and Directionality of the Earth's Reflectances instrument (POLDER, Buriez et al., 1997).

The contrast of brightness temperatures measured at two wavelengths is related to the ice volume fraction due to the different emissivity of ice and liquid water at wavelengths larger than 10 μm. In the same way the cloud reflectance at NIR wavelengths is affected by the different refractive indices (in particular the imaginary part, i.e. absorption index) of ice and liquid water as demonstrated by Pilewskie and Twomey (1987). Therefore, the ratio of cloud reflectance at two wavelengths was used to determine the cloud thermodynamic phase (band ratio method). Both methods were compared by Chylek et al. (2006) for the Moderate Resolution Imaging Spectroradiometer (MODIS) showing significant discrepancies between the results of the two methods with a tendency of an overprediction of ice phase by the band ratio method. The authors suggest to use the ratio of NIR high resolved spectral bands around 1.5 and 1.4 μm. This was applied successfully by Knap et al. (2002) and Acarreta et al. (2004) for the Airborne Visible and Infrared Imaging Spectrometer (AVIRIS) and the Scanning Imaging Absorption Spectrometer for Atmospheric CHartographY (SCIAMACHY).

In this study we present similar methods of cloud phase identification using airborne spectral solar cloud reflectance measurements combined with radiative transfer simulations. Three approaches to discriminate the cloud phase are applied and discussed.

ACPD
8, 15901–15939, 2008

First results for cloud phase identification with the SMART-Albedometer were published in Ehrlich et al. (2008a). The measurements presented here were performed during the Arctic Study of Tropospheric Aerosol, Clouds and Radiation (ASTAR) 2007 campaign. Additional information on cloud phase was obtained from in situ cloud microphysical and airborne lidar measurements.

The instrumentation of the aircraft is described in Sect. 2. The measurements of spectral cloud reflectance and three methods to obtain information on the cloud phase are discussed in Sects. 3 and 4. Subsequently, the three methods are analyzed by sensitivity studies in Sect. 5. Finally in Sect. 6 the application of the methods is examined by a case study of observations from 7 April 2007.

2 Instrumentation

During ASTAR 2007 two aircraft were employed. We report on data from the Polar 2 aircraft, owned by the Alfred Wegener Institute for Polar and Marine Research (AWI). The airborne instrumentation included the Spectral Modular Airborne Radiation measurement sysTem (SMART-Albedometer), in situ instruments such as the Polar Nephelometer, Cloud Particle Imager (CPI), and Particle Measuring System (PMS) Forward Scattering Spectrometer Probe (FSSP-100), and the Airborne Mobile Aerosol Lidar (AMALi).

The SMART-Albedometer was developed at the Leibniz-Institute for Tropospheric Research as a modular system to measure solar spectral radiation (radiance, irradiance, actinic radiation) from airborne platforms as described e.g. by (Wendisch and Mayer, 2003; Wendisch et al., 2004; Jäkel et al., 2005, Bierwirth et al., 2008[1]). The

[1]Bierwirth, E., Wendisch, M., Ehrlich, A., Heese, B., Tesche, M., Althausen, D., Schladitz, A., Müller, D., Otto, S., Trautmann, T., Dinter, T., von Hoyningen-Huene, W., and Kahn, R.: Spectral surface albedo over Morocco and its impact on the radiative forcing of Saharan dust, Tellus, 61B, submitted, 2008.

optical inlets for separate detection of upwelling and downwelling radiation are actively leveled to compensate deviations of the aircraft attitude from the horizontal plane (Wendisch et al., 2001). The configuration of the SMART-Albedometer operated during ASTAR 2007 provides measurements of downwelling and upwelling spectral irradiances ($F_\lambda^\downarrow$, $F_\lambda^\uparrow$) simultaneously with upwelling nadir spectral radiance ($I_\lambda^\uparrow$). Two spectrometer systems were applied to measure $F_\lambda^\downarrow$ and $I_\lambda^\uparrow$ covering the visible (350–950 nm) and near infrared wavelength range (950–2100 nm) with a spectral resolution (full width at half maximum) of 2–3 nm and 9–16 nm. $F_\lambda^\uparrow$ was measured in the visible part of the spectrum only (350–950 nm). The optical inlets for the irradiance measurements constructed by the Bay Area Environmental Research Institute, CA, USA were designed as integrating spheres made of Spectralon reflectance material (Crowther, 1997). Sealed with a quartz dome the Spectralon integrating sphere provides an almost wavelength independent photon collection efficiency. To measure $I_\lambda^\uparrow$ a set of new optical inlets for radiance measurements was constructed. The entrance optics of the radiance optical inlet is based on a Zeiss collimator lens (BK 7 glass) with a focal length of 31.6 mm. The collimator is mounted within a cylindrical housing reducing stray light. Two opening apertures at both ends of the housing define the angle of view. Laboratory measurements and ray tracing simulations found an angle of view of 1.5°. The outer aperture is covered by BK 7 glass providing vacuum conditions inside the tube and protection against condensation during changes of the external temperature conditions.

The in situ measurements of cloud microphysical properties include particle number size distribution, extinction coefficient, ice and liquid water content, effective diameter, scattering phase function and the asymmetry parameter, a measure for the anisotropy of the scattering phase function. The instruments, data retrieval and measurement uncertainties are described by Gayet et al. (2007).

Additional independent information on the cloud phase was provided by the depolarization measurements of AMALi which is a two-wavelength (532 nm and 355 nm) backscatter lidar with depolarization measurements at 532 nm wavelength. AMALi was installed in nadir looking configuration. The vertical resolution amounts to 7.5 m. The minimum horizontal resolution was around 900 m. Further details of AMALi are described in Stachlewska et al. (2004).

3 Measurements

During ASTAR 2007 (7–9 April) a cold air outbreak with northerly winds initiated extended boundary layer cloud fields over the open Greenland Sea as shown by the MODIS satellite image in Fig. 1. The convection above the relatively warm open sea maintained the coexistence of ice and liquid water in these clouds. Detailed investigations on the self maintaining dynamics of the mixed-phase clouds are described by Harrington et al. (1999); Fridlind et al. (2007); Morrison et al. (2008). In addition to the predominating mixed-phase clouds, pure ice and pure liquid water clouds were observed during ASTAR 2007 providing the possibility to test cloud phase identification methods.

3.1 In situ measurements

In situ observations of the prevailing mixed-phase clouds showed a cloud top layer typically consisting of liquid water with precipitating ice below (Fig. 2). The FSSP indicated particle concentrations up to N_{tot}=50 cm^{-3} between 1000–1700 m altitude. In the same layers the asymmetry parameter obtained by the Polar Nephelometer, was about 0.85 which is a typical value for spherical liquid water droplets (e.g. Gerber et al., 2000). A narrow ice layer was found between 800 m and 1100 m indicated by lower asymmetry parameters and particle concentrations measured by the CPI up to N_{tot}=1.5 cm^{-3}. Below this, precipitating large ice particles were observed down to 500 m. For ice crystals and liquid water particles mean effective diameters of (85±37) μm and (15±5) μm were measured. The cloud optical thickness estimated from the measured extinction coefficients was about 15–20.

3.2 Airborne lidar measurements

The laser of the AMALi lidar did not penetrate the optically thick clouds completely. However, AMALi did identify a liquid water layer at cloud top from the depolarization signal. Although multiple scattering in the liquid water layer generated high depolarization values comparable to the depolarization signal of ice crystals the detailed analysis of the lidar profiles averaged over 15 s reveals differences in the vertical pattern of the depolarization. The depolarization related to multiple scattering of liquid water particles increases slowly with cloud depth whereas nonspherical ice crystals result in an instantaneous increase of the depolarization (Hu et al., 2007). From this analysis the precipitating ice below the clouds could be identified in several cloud gaps.

3.3 Cloud top reflectance

Spectral cloud top reflectances $R_\lambda = \pi \cdot I_\lambda^\uparrow / F_\lambda^\downarrow$ were calculated from the SMART-Albedometer radiance and irradiance measurements. Beside the typical mixed-phase clouds also pure ice and pure liquid water clouds could be observed during ASTAR 2007. Cloud top reflectances for all three measured cloud types shown in Fig. 3a reveal differences in the spectral pattern of R_λ in the wavelength range 1450–1750 nm. These differences are caused by the contrast in the imaginary part n_i of the refractive index (absorption index) of ice and liquid water shown in Fig. 3b. Of all clouds, pure liquid water clouds show the highest R_λ values at 1500 nm where the difference of ice and liquid water absorption is maximum. The slope of the reflectance between 1500 nm and 1750 nm is small for liquid water clouds and larger for pure ice clouds. These differences in the spectral pattern of R_λ can be used to remotely discriminate the cloud phase.

ACPD

8, 15901–15939, 2008

4 Definition of ice indices: three approaches

To define and evaluate the sensitivity of the ice indices we performed radiative transfer simulations for pre-defined pure ice and pure liquid water boundary layer clouds of various optical thickness (τ=2–20) and effective diameter D_{eff}. For liquid water clouds the effective diameter was chosen between 8 μm and 26 μm corresponding to the range reported by Miles et al. (2000) for marine stratocumulus clouds. The ice clouds were modeled for the range of effective diameter observed during ASTAR 2007 (30–150 μm).

The spectral solar radiative transfer simulations were performed with the libRadtran (Library for Radiative transfer) code by Mayer and Kylling (2005) for the wavelength range 300 nm to 2200 nm adapted to the spectral resolution of the SMART-Albedometer measurements. The discrete ordinate solver DISORT version 2.0 by Stamnes et al. (1988) was applied. The meteorological input (profiles of static air temperature, relative humidity and static air pressure) was composed of a radio sounding at Ny Ålesund/Svalbard (7 April 2004, 11:00 UTC). Corresponding to the observed marine clouds the surface albedo was represented by measurements above sea water obtained during ASTAR 2007.

The stratiform cloud layer was situated between 750 m and 1750 m altitude above the sea surface. The cloud optical properties (extinction coefficient, single scattering albedo and scattering phase function) were calculated from optical properties of the individual cloud particles. Mie-theory was applied for liquid water droplets. For the ice particles column shaped ice crystals were selected. The optical properties of columns were provided by Yang and Liou (1996) based on a combination of methods including an Improved Geometric Optics Method (IGOM) for nonspherical ice crystals.

Results of the radiative transfer simulations for clouds comparable to the observed ice, liquid water and mixed-phase clouds (τ=12) are given in Fig. 4. The simulations of R_λ show a similar spectral pattern in the wavelength range 1450–1750 nm compared to the measurements of the three cloud types (Fig. 3a) with the steepest slope observed for the ice cloud. For wavelengths shorter than 1300 nm, R_λ differs in the simulations

ACPD
8, 15901–15939, 2008

Title Page
Abstract Introduction
Conclusions References
Tables Figures
◀ ▶
Back Close
Full Screen / Esc
Printer-friendly Version
Interactive Discussion

because of the different scattering phase functions of ice (nonspherical shape) and liquid water particles (spherical shape).

The characteristics of the reflectance spectra were used in the following three approaches to retrieve the cloud phase from the measurements. A common two-wavelengths approach and a principle component analysis was applied. A third approach used the combined albedo and reflectance measurements to obtain information on the cloud phase.

4.1 Two-wavelengths approach

The spectral slope of the cloud reflectance between 1640 nm and 1700 nm was used to identify the cloud phase with AVIRIS by Knap et al. (2002). The dimensionless ice index defined as $I_S^{Knap}=(R_{1700\,nm}-R_{1640\,nm})/R_{1640\,nm}\cdot 100$ vanishes for pure liquid water clouds and reaches values of up to 30 for pure ice clouds. For SCIAMACHY Acarreta et al. (2004) increased the wavelength range of interest to 1550–1670 nm. The spectral slope was calculated by linear regression excluding the absorption bands of CO_2. Ice indices calculated this way range between 10 for liquid water clouds and 50 for ice clouds.

The wavelength range used by Acarreta et al. (2004) was limited to 1670 nm due to technical characteristics of SCIAMACHY with changing spectral resolution at 1670 nm. For our measurements with the SMART-Albedometer the definition of ice index I_S was extended to the wavelength range 1550–1700 nm,

$$I_S = \frac{100}{R_{1640\,nm}} \left[\frac{dR_\lambda}{d\lambda}\right]_{1550-1700\,nm} \quad (1)$$

This is the maximum wavelength range where water vapor absorption does not contribute significantly to the measured signal. To reduce the impact of noise from the individual wavelength channels the slope of R_λ was calculated by linear regression. Wavelengths affected by CO_2 absorption were excluded from the regression (1560–1580 nm and 1595–1610 nm).

ACPD
8, 15901–15939, 2008

The ice index I_S calculated from the three measured clouds presented in Fig. 3a are given in Table 1. The values range from 8.8 for the liquid water cloud to 57 for the ice cloud with the mixed-phase cloud in-between. These significant differences in I_S confirm that the three observed clouds (pure ice, pure liquid water and mixed-phase) can be distinguished with this method. I_S calculated from the simulated ice and liquid water clouds is shown in Fig. 5. Typical values for liquid water clouds range between I_S=5 and I_S=15. Ice clouds show a higher variability of I_S with values of up to 80.

4.2 Principle component analysis

Principle component analysis (PCA) provides a powerful tool to understand the variations in a multivariate data set (Pearson, 1901). The transformation of the original data into a set of principle components reduces the information given by the multivariate data to a few principle components. Analyzing spectral atmospheric radiation measurements the obtained principle components are correlated with physical processes like molecular scattering, trace gas absorption or aerosol interaction (Rabbette and Pilewskie, 2001). We utilized the PCA to extract the ice and liquid water absorption signature in the spectral cloud top reflectance.

PCA was applied separately on the simulated pure ice and pure liquid water boundary layer clouds introduced above (τ=2/4/6/8/10/12/14/16/18/20). For the ice clouds simulations for D_{eff}=30/60/90/120/150 μm were considered in the PCA providing a set of 50 different clouds. In the PCA of the water cloud simulations D_{eff}=8/10/14/20/26 μm were included. The simulated cloud top reflectance was normalized with $R_{860\,\text{nm}}$ to eliminate the impact of cloud optical depth. To focus on the ice and liquid water absorption signature the wavelength range between 1500 nm and 1800 nm was considered for the calculations only. Finally the principle components PC_i were calculated by applying the component weightings $\gamma_{i,\lambda}$ obtained form the PCA with,

$$\mathrm{PC}_i = \sum_{\lambda=1500\,\mathrm{nm}}^{1800\,\mathrm{nm}} \gamma_{i,\lambda} \frac{R_\lambda}{R_{860\,\mathrm{nm}}}. \tag{2}$$

Due to the normalization with $R_{860\,\mathrm{nm}}$ the remaining variance of the data will mainly result from the absorption of the particles due to the variation of their effective diameter. Consequently the calculations showed that the first principle component derived from the pure liquid water cloud simulations is related to liquid water absorption. The contribution of R_λ at individual wavelengths to PC_W is given by the component weightings γ_W shown in Fig. 6. The minimum weight occurs in the wavelengths between 1600 nm and 1700 nm where liquid water absorption is weak as indicated by the imaginary part n_i of the refractive index (dashed line). In the same way the first principle component from the pure ice cloud simulations PC_I is correlated with ice absorption and has the maximum component weighting γ_I at wavelengths around 1550 nm. To utilize PC_W and PC_I for cloud phase identification we defined a respective ice index I_P as,

$$I_\mathrm{P} = \left(\frac{PC_\mathrm{I}}{PC_\mathrm{W}} - 0.57\right) \cdot 100. \tag{3}$$

The subtraction of 0.57 was chosen arbitrarily to obtain values close to zero for liquid water clouds. For the observed liquid water cloud presented in Fig. 3a I_P=0.6 was calculated. Values for all three observed clouds are given in Table 1. The results of the analysis of the simulated liquid water clouds shown in Fig. 7 reveal typical values of I_P=0–2. For ice clouds I_P ranges from values of 4 up to 20 clearly capable of being distinguished from liquid water clouds.

4.3 Albedo-reflectance

In general clouds act as non-lambertian reflectors. The radiance field reflected from cloud top is essentially affected by the anisotropic scattering phase function of the cloud particles. Representative scattering phase functions for spherical liquid water particles and ice crystals of column, plate and aggregate shape are illustrated in Fig. 8. Chepfer et al. (2002) used this information to retrieve the ice crystal shape from dual satellite measurements at the wavelength of 650 nm. From the differences in the radiation scattered close to the backscatter angle of 180° and those scattered into viewing angles between 60° and 150° particle phase and shape can be distinguished. A similar retrieval of particle phase and shape was applied by McFarlane et al. (2005) to measurements of the Multiangle Imaging Spectroradiometer (MISR) using the nine different viewing angles of the instrument. By minimizing the differences between measured and simulated reflectances they were able to calculate an ice index. It was shown that the highest differences between droplets and crystals occur between 70° and 130° scattering angle. Both studies emphasize that the retrieved properties are representative only for particles near cloud top.

The configuration of the SMART-Albedometer operating under conditions of low Sun allows for a similar retrieval of the cloud phase using simultaneous albedo and nadir reflectance measurements. With the high solar zenith angles (70° to 85°) present during ASTAR 2007, the nadir reflectance measurements correspond to side scattering by the cloud particles with scattering angles of 95° to 110° assuming single scattering as being predominant. As indicated by the grey area in Fig. 8 this scattering angles provide substantially enhanced scattering by nonspherical particles compared to spherical particles. This increases the measured upwelling radiance and cloud reflectance which is confirmed by the simulations shown in Fig. 4. The pure ice cloud shows higher R_λ at wavelengths up to 1300 nm than the simulations for the pure liquid water cloud. On the other hand, the upwelling irradiance and consequently the albedo $\alpha_\lambda = F_\lambda^\uparrow / F_\lambda^\downarrow$ includes information from all scattering angles and is less dependent on the scattering phase function. This is illustrated in Fig. 9 by comparison of R_λ and α_λ measured above the mixed-phase and pure ice cloud observed on 7 April 2007. Both clouds had a similar optical thickness of 12. The measurements show, that the difference between R_λ and α_λ are smaller for the ice cloud compared to the mixed-phase cloud, where liquid water

ACPD
8, 15901–15939, 2008

was found at cloud top.

From this assumptions we suggest the ratio of cloud top reflectance to albedo at 645 nm wavelength $\beta_\mathrm{I}=R_{645\,\mathrm{nm}}/\alpha_{645\,\mathrm{nm}}$ as an indicator of the anisotropy of the radiation field reflected at cloud top. For solar zenith angles larger than 60° nonspherical particles give a higher β_I than spherical particles. Increasing cloud optical depth also increases β_I due to multiple scattering processes.

From the simulation of pure liquid water clouds and pure ice clouds presented above β_I was calculated and plotted as a function of the corresponding $R_{645\,\mathrm{nm}}$ (Fig. 10). Both liquid water and ice clouds show a distinct relation between β_I and $R_{645\,\mathrm{nm}}$, with the isotropy of the reflected radiation being significantly higher above ice clouds compared to the liquid water clouds of the same $R_{645\,\mathrm{nm}}$. These differences can be utilized to identify the cloud phase.

Calculating the deviation of measured β_I to the theoretical β_I values of pure liquid water clouds of the same $R_{645\,\mathrm{nm}}$ gives an indicator for the cloud phase. The ice index I_A was defined as the ratio

$$I_\mathrm{A} = \frac{\beta_\mathrm{I}^{\mathrm{meas}}}{\beta_\mathrm{I}^{\mathrm{water}}(R_{645\mathrm{nm}}^{\mathrm{meas}})}. \tag{4}$$

Interpolated values of $\beta_\mathrm{I}^{\mathrm{water}}$ are derived by the polynomial fit shown as blue solid line in Fig. 10. From the definition of I_A it follows that we obtain $I_\mathrm{A}=1$ for pure liquid water clouds and $I_\mathrm{A}>1$ for pure ice clouds.

The results for the observed pure ice cloud and mixed-phase cloud shown in Fig. 3a are given in Table 1. Both values differ significantly from one. For the pure liquid water cloud it was not possible to calculate I_A. This cloud had a small horizontal extension. The measured albedo was substantially affected by the dark water surface visible apart the cloud.

Typical values for water clouds obtained from the simulated clouds are shown in Fig. 11 and range between $I_\mathrm{A}=0.98$ and $I_\mathrm{A}=1.03$. Ice clouds give higher values of $I_\mathrm{A}>1.06$ separated distinctly from the results for liquid water clouds.

5 Sensitivity studies

The cloud top reflection (especially in the wavelength range used to calculate the ice indices) is affected not only by the cloud thermodynamic phase but also by other cloud optical properties (cloud optical depth and cloud particle effective diameter). In order to reduce their impact on the cloud phase retrieval we applied different normalizations of R_λ before calculating the ice indices as shown above. Nevertheless it is impossible to overcome those related uncertainties completely.

Acarreta et al. (2004) showed for their ice index similar to I_S that the ice index of ice clouds may vary by a factor of up to 3 between clouds of small effective diameter/low cloud optical thickness and clouds of large effective diameter/high cloud optical thickness. Changes in the solar zenith angle were found to be less important for the simulated ice indices. Especially for optically thin clouds the surface properties will have an impact on the ice indices. The surface albedo is crucial for the visible wavelength used to calculate I_A while absorption by liquid water, snow or sea ice may affect I_S and I_P. In order to reduce the complexity in this study we concentrate on the conditions found during ASTAR 2007 with open sea as surface.

In the following we discuss the impact of cloud optical depth and particle effective diameter for the ice indices defined in this paper (Sect. 5.1). Section 5.2 presents investigations of the sensitivity of the ice indices on the vertical structure of mixed-phase clouds.

5.1 Cloud optical properties

The ice indices I_S, I_P and I_A calculated from the simulations of pure ice and liquid water clouds of different τ and D_{eff} are shown in Figs. 5, 7 and 11. The plots reveal that the ice indices are almost insensitive to D_{eff} and τ for pure liquid water clouds. The values vary only slightly with D_{eff} and τ. I_P and I_A show almost no variation with τ. On the other hand, the ice indices of the pure ice clouds spread over a wide range. Most significant is the decrease of I_S and I_P with decreasing D_{eff}. Especially for optical thin ice clouds I_S can reach values of pure liquid water clouds. A slight improvement is given by I_P. Here non of the ice clouds give values as low as the simulated liquid water clouds. Nevertheless in order to achieve a reliable identification of ice, liquid water and especially mixed-phase clouds from I_S and I_P a priori knowledge about the ice crystal effective diameter and the cloud optical depth is needed.

Most robust with regard to the cloud optical properties of ice crystals is the ice index I_A. Figure 11 shows that values for ice and liquid water clouds differ for all simulations. Therefore I_A is most suitable for discriminating ice and liquid water clouds in the setting of the present sensitivity study.

5.2 Vertical distribution

A second sensitivity study focuses on the ability to identify mixed-phase clouds typically consisting of two layers with liquid water droplets at cloud top and precipitating ice below. Radiative transfer simulations were performed based on the microphysical measurements on 7 April 2007 presented in Sect. 3. The cloud optical properties were fixed at τ=15, D_{eff}=15 μm for liquid water particles and D_{eff}=85 μm for ice particles. The cloud was divided into 10 sublayers with a homogeneous liquid water mode of τ_W=1.5 for each layer. One ice layer (τ_I=1.5) was added and shifted from cloud top to cloud bottom. For each simulation the ice indices I_S, I_P and I_A were calculated. The results are given in Table 2.

The results show that all three indices are most sensitive to the upper cloud layer showing the highest values if the ice layer is located at cloud top (τ_W^{top}=0). Here τ_W^{top} gives the total optical depth of the liquid water layers located above the single ice layer. The maximum values of I_S=42, I_P=7.8 and I_A=1.08 range above typical values for pure liquid water clouds (cf. Figs. 5, 7 and 11). I_S and I_P decrease slowly with increasing τ_W^{top} to values of I_S=12, I_P=1.6 which reaches the range simulated for pure water clouds. Nevertheless, for τ_W^{top}<10 and considering the effective diameter of the water particles (D_{eff}=15 μm) the ice indices I_S and I_P are higher than for pure liquid water clouds. This

ACPD
8, 15901–15939, 2008

suggests that these approaches are able to distinguish typical boundary layer mixed-phase clouds with a liquid cloud top layer from pure liquid water clouds.

The ice index I_A deviates from values of pure liquid water clouds only if the ice layer is at cloud top. This suggests that I_A is suitable only for pure ice clouds. Typical boundary layer mixed-phase clouds with liquid cloud top will be identified as pure liquid water clouds. This is consistent with the findings of Chepfer et al. (2002) who found that particle shape retrieved from two scattering angles at 650 nm wavelength was insensitive to multilayered clouds when τ of the cloud top layer is larger than 2.

6 Case study on 7 April 2007

On 7 April 2007 concurrent radiation and microphysical measurements were conducted along the path of the Cloud-Aerosol Lidar and Infrared Pathfinder Satellite (CALIPSO) over the Greenland sea as shown in Fig. 1. A stratus cloud field with cloud top up to 1500 m extended from 77.3° N) to northern areas at the time of the CALIPSO overpass (10:18 UTC). The profile of total attenuated backscatter signal measured by CALIPSO is shown in Fig. 12a. The lidar could not completely penetrate the optically thick clouds with exception of the cloud edge (<77.4° N). For the investigated cloud the depolarization measurements (not shown here) were not suitable for a cloud phase analysis. Multiple scattering in the optically thick clouds increased the depolarization regardless of particle shape. Nevertheless the lidar profiles reveal that in the southern part of the cloud deck (see Fig. 1 and left-side of Fig. 12a) ice particles are precipitating down to the surface. These precipitation particles, which are also observed from CloudSat (reflectivity), can be detected by the Lidar because they are not capped by a liquid water layer in this area.

This part of the cloud was sampled with in situ microphysical instruments about 1 h before the CALIPSO overpass. Considering the advection of the cloud field with the northerly winds the measurements showed that the cloud edge in the southern part consisted of ice particles only (Fig. 12b, <77.4° N). The particle concentration measured by the CPI increases up to N_{tot}=3 cm^{-3}. First liquid water particles were observed with the FSSP 3 km further north. After the descent below cloud base (77.5° N to 77.6° N) the partly high ice crystal concentrations with simultaneous absence of liquid water particles is related again to precipitating ice below the cloud. Higher cloud layers are probably of mixed-phase as measured during the ascent through the cloud (77.6° N to 77.7° N).

Shortly after the CALIPSO overpass the cloud was investigated again by radiation measurements flying above the cloud top. From the measured cloud top reflectance the cloud phase was remotely identified using the ice indices defined above. Figure 12c shows the measured ice indices I_S and I_P along the flight track of 7 April 2007. Both ice indices show high values around 77.4° N correlated with the high ice particle concentration measured from the in situ instrumentation 1 h before. The maximum values I_S=60 and I_P=13 indicate a pure ice cloud. Lower values (I_S=20–40 and I_P=5–10) corresponding to mixed-phase clouds were measured afterwards when the FSSP measured significant liquid water particle concentrations. With respect to the sensitivity studies of Sect. 5 I_S and I_P measured above the mixed-phase clouds are higher than expected and close to values of pure ice clouds with small effective diameter. This reveals that either the fraction of ice crystals is much higher than measured by the in situ measurements or the vertical distribution of the ice differs from the assumption of a liquid cloud top layer with high ice concentrations below.

The analysis of the reflectance-albedo ratio β_I also reveals the presence of ice at the cloud edge. Figure 13 shows all measurements taken on 7 April 2007 above clouds. Generally the measured values of β_I deviate from the theoretical curve of pure liquid water clouds (1-D simulations) which is not expected for mixed-phase clouds with a thick liquid layer at cloud top (cp. Sect. 5.2). The high values of β_I indicate the presence of ice crystals at the top of the mixed-phase clouds. It has to be pointed out here that due to the combination of three single measurements ($F_\lambda^\downarrow$, $F_\lambda^\uparrow$ and $I_\lambda^\uparrow$) the uncertainties of the data points are relatively high as marked at two measurements samples in Fig. 13. Furthermore the 1-D-simulations used to define I_A do not account for possible

3-D radiative effects. Nevertheless the measurements above the cloud edge (labeled by red crosses) tend to range in higher values of β_{I}. This shows that at the cloud edge nonspherical ice crystals were present at cloud top.

7 Conclusions

Three different methods to derive the cloud thermodynamic phase from airborne spectral solar radiation measurements were presented. The ice index I_{S} analyzing the slope of the spectral reflectance and the ice index I_{P} obtained from PCA are capable to identify the cloud phase of low level boundary layer clouds observed during ASTAR 2007. Within a case study a pure ice cloud at the edge of a mixed-phase cloud field also probed by in situ microphysical probes and observed by CALIPSO showed significant higher values of I_{S} and I_{P} related to ice particles. The mixed-phase clouds inside the cloud field showed lower ice indices compared to the ice cloud but higher values than expected for pure liquid water clouds.

The third ice index I_{A} based on the anisotropy of the reflected radiation and defined by the ratio between cloud reflectance and albedo is not able to detect mixed-phase clouds. Simulations showed that I_{A} is mainly affected by the uppermost cloud layers. The optical thickness of the relevant cloud layer was found to be less than τ<1.5. Therefore mixed-phase clouds with liquid cloud top will be identified as pure liquid clouds. Nevertheless for the edge of the cloud field the presence of nonspherical ice crystals was confirmed.

At least for the cloud top layer I_{A} is theoretically a more distinct indicator for the cloud phase than I_{S} and I_{P}. Sensitivity studies showed that both indices I_{S} and I_{P} are strongly dependent on the ice particle effective diameter. Pure ice clouds with small ice crystals result in I_{S} and I_{P} close to values of pure liquid water clouds. Therefore, the discrimination of mixed-phase and ice clouds requires a priori knowledge about the ice crystal dimensions. Cloud optical depth has a minor impact on all three ice indices relevant for clouds with τ<5.

The case study showed, that I_A is more difficult to interpret compared to I_S and I_P. The combination of three independent measurements and possible 3-D radiative effects result in a higher uncertainty of this method. From a single measuring point the retrieval of ice phase is not reliable. Cluster analysis or averaging is necessary.

Considering the advantages and uncertainties of all three methods we suggest to rely on a combination of the methods in further studies. Together with airborne lidar and in situ microphysical measurements as presented here further investigations will help to verify algorithms for cloud phase identification from satellites (CALIPSO, CloudSat, MODIS). Especially airborne hyperspectral camera systems resolving the near infrared wavelength range will be capable to investigate the detailed horizontal distribution of ice and liquid water particles.

Acknowledgements. This research was funded by the German Research Foundation (DFG, WE 1900/8-1) and AWI. We thank Ping Yang, Department of Atmospheric Sciences at Texas A&M University, for providing the library of optical properties of ice crystals used in our simulations. Bernhard Mayer (Institute of Atmospheric Physics, German Aerospace Center) is thanked for his support with the libRadtran package. The CALIPSO data presented here were courtesy of the NASA Langley Research Center Atmospheric Science Data Center. For the technical support during the ASTAR campaign we want to acknowledge the companies *enviscope* GmbH and OPTIMARE GmbH.

References

Acarreta, J. R., Stammes, P., and Knap, W. H.: First retrieval of cloud phase from SCIAMACHY spectra around 1.6 μm, Atmos. Res., 72, 89–105, 2004. 15904, 15910, 15915

Boudala, F. S., Isaac, G. A., Cober, S. G., and Fu, Q.: Liquid fraction in stratiform mixed-phase clouds from in situ observations, Q. J. Roy. Meteorol. Soc., 130, 2919–2931, 2004. 15903

Buriez, J., Vanbauce, C., Parol, F., Goloub, P., Herman, M., Bonnel, B., Fouquart, Y., Couvert, P., and Seze, G.: Cloud detection and derivation of cloud properties from POLDER, Int. J. Rem. Sens., 18, 2785–2813, 1997. 15904

Chepfer, H., Minnis, P., Young, D., Nguyen, L., and Arduini, R. F.: Estimation of cirrus cloud

effective ice crystal shapes using visible reflectances from dual-satellite measurements, J. Geophys. Res.-Atmos., 107, 4730, doi:10.1029/2000JD000240, 2002. 15913, 15917
Chylek, P., Robinson, S., Dubey, M. K., King, M. D., Fu, Q., and Clodius, W. B.: Comparison of near-infrared and thermal infrared cloud phase detections, J. Geophys. Res.-Atmos., 111, D20203, doi:10.1029/2006JD007140, 2006. 15904
Cober, S. G., Isaac, G. A., Korolev, A. V., and Strapp, J. W.: Assessing cloud-phase conditions, J. Appl. Meteorol., 40, 1967–1983, 2001. 15904
Corell, R.: Arctic Climate Impact Assessment, Cambridge University Press, Cambridge, UK, 2004. 15903
Crowther, B.: The Design, Construction, and Calibration of a Spectral Diffuse/Global Irradiance Meter, Ph.D. thesis, University of Arizona, 1997. 15906
Curry, J. A., Rossow, W. B., Randall, D., and Schramm, J. L.: Overview of Arctic cloud and radiation characteristics, J. Climate, 9, 1731–1764, 1996. 15903
Dong, X. Q. and Mace, G. G.: Arctic stratus cloud properties and radiative forcing derived from ground-based data collected at Barrow, Alaska, J. Climate, 16, 445–461, 2003. 15903
Ehrlich, A., Bierwirth, E., Wendisch, M., Gayet, J.-F., Mioche, G., and Richter, A.: Cloud phase identification over Arctic mixed-phase clouds from airborne spectral cloud top reflectance measurements, in: Proceedings of the ICCP Conference, Cancun, Mexico, 7–11 July 2008a. 15905
Ehrlich, A., Wendisch, M., Bierwirth, E., Herber, A., and Schwarzenböck, A.: Ice crystal shape effects on solar radiative properties of Arctic mixed-phase clouds – Dependence on microphysical properties, Atmos. Res., 88, 266–276, 2008b. 15903
Freese, D. and Kottmeier, C.: Radiation exchange between stratus clouds and polar marine surfaces, Bound.-Lay. Meteorol., 87, 331–356, 1998. 15903
Fridlind, A. M., Ackerman, A. S., McFarquhar, G., Zhang, G., Poellot, M. R., DeMott, P. J., Prenni, A. J., and Heymsfield, A. J.: Ice properties of single-layer stratocumulus during the Mixed-Phase Arctic Cloud Experiment: 2. Model results, J. Geophys. Res.-Atmos., 112, D24202, doi:10.1029/2007JD008646, 2007. 15907
Gayet, J.-F., Stachlewska, I. S., Jourdan, O., Shcherbakov, V., Schwarzenboeck, A., and Neuber, R.: Microphysical and optical properties of precipitating drizzle and ice particles obtained from alternated Lidar and in situ measurements, Ann. Geophys., 25, 1487–1497, 2007, http://www.ann-geophys.net/25/1487/2007/. 15906
Gerber, H., Takano, Y., Garrett, T. J., and Hobbs, P. V.: Nephelometer measurements of the

ACPD
8, 15901–15939, 2008

Title Page
Abstract | Introduction
Conclusions | References
Tables | Figures
◀◀ | ▶▶
◀ | ▶
Back | Close
Full Screen / Esc
Printer-friendly Version
Interactive Discussion

asymmetry parameter, volume extinction coefficient, and backscatter ratio in Arctic clouds, J. Atmos. Sci., 57, 3021–3034, 2000. 15907

Harrington, J. Y., Reisin, T., Cotton, W. R., and Kreidenweis, S. M.: Cloud resolving simulations of Arctic stratus – Part II: Transition-season clouds, Atmos. Res., 51, 45–75, 1999. 15903, 15907

Hu, Y., Vaughan, M., Liu, Z., Lin, B., Yang, P., Flittner, D., Hunt, B., Kuehn, R., Huang, J., Wu, D., Rodier, S., Powell, K., Trepte, C., and Winker, D.: The depolarization attenuated backscatter relation: CALIPSO lidar measurements vs. theory, Optics Express, 15, 5327–5332, 2007. 15908

Intrieri, J. M., Fairall, C. W., Shupe, M. D., Persson, P. O. G., Andreas, E. L., Guest, P. S., and Moritz, R. E.: An annual cycle of Arctic surface cloud forcing at SHEBA, J. Geophys. Res.-Oceans, 107, 8039, doi:10.1029/2000JC000439, 2002. 15903

Jäkel, E., Wendisch, M., Kniffka, A., and Trautmann, T.: Airborne system for fast measurements of upwelling and downwelling spectral actinic flux densities, Appl. Optics, 44, 434–444, 2005. 15905

Key, J. and Intrieri, J.: Cloud particle phase determination with the AVHRR, J. Appl. Meteorol., 39, 1797–1804, 2000. 15904

King, M. D., Platnick, S., Yang, P., Arnold, G. T., Gray, M. A., Riedi, J. C., Ackerman, S. A., and Liou, K. N.: Remote sensing of liquid water and ice cloud optical thickness and effective radius in the Arctic: Application of airborne multispectral MAS data, J. Atmos. Oceanic Technol., 21, 857–875, 2004. 15904

Knap, W., Stammes, P., and Koelemeijer, R.: Cloud thermodynamic-phase determination from near-infrared spectra of reflected sunlight, J. Atmos. Sci., 59, 83–96, 2002. 15904, 15910

Kokhanovsky, A. A., Rozanov, V. V., Nauss, T., Reudenbach, C., Daniel, J. S., Miller, H. L., and Burrows, J. P.: The semianalytical cloud retrieval algorithm for SCIAMACHY – I. The validation, Atmos. Chem. Phys., 6, 1905–1911, 2006, http://www.atmos-chem-phys.net/6/1905/2006/. 15904

Korolev, A. V., Isaac, G. A., Cober, S. G., Strapp, J. W., and Hallett, J.: Microphysical characterization of mixed-phase clouds, Q. J. Roy. Meteorol. Soc., 129, 39–65, 2003. 15903

Lawson, R. P., Baker, B. A., Schmitt, C. G., and Jensen, T. L.: An overview of microphysical properties of Arctic clouds observed in May and July 1998 during FIRE ACE, J. Geophys. Res.-Atmos., 106, 14 989–15 014, 2001. 15904

Mayer, B. and Kylling, A.: Technical note: The libRadtran software package for radiative transfer

calculations – description and examples of use, Atmos. Chem. Phys., 5, 1855–1877, 2005, http://www.atmos-chem-phys.net/5/1855/2005/. 15909
McFarlane, S. A., Marchand, R. T., and Ackerman, T. P.: Retrieval of cloud phase and crystal habit from Multiangle Imaging Spectroradiometer (MISR) and Moderate Resolution Imaging Spectroradiometer (MODIS) data, J. Geophys. Res.-Atmos., 110, D14201, doi:10.1029/2004JD004831, 2005. 15913
McFarquhar, G. M., Zhang, G., Poellot, M. R., Kok, G. L., Mccoy, R., Tooman, T., Fridlind, A., and Heymsfield, A. J.: Ice properties of single-layer stratocumulus during the Mixed-Phase Arctic Cloud Experiment: 1. Observations, J. Geophys. Res.-Atmos., 112, D24201, doi:10.1029/2007JD008633, 2007. 15904
Miles, N. L., Verlinde, J., and Clothiaux, E. E.: Cloud droplet size distributions in low-level stratiform clouds, J. Atmos. Sci., 57, 295–311, 2000. 15909
Morrison, H., Pinto, J. O., Curry, J. A., and McFarquhar, G. M.: Sensitivity of modeled arctic mixed-phase stratocumulus to cloud condensation and ice nuclei over regionally varying surface conditions, J. Geophys. Res.-Atmos., 113, D05203, doi:10.1029/2007JD008729, 2008. 15907
Pearson, K.: On lines and planes of closest fit to systems of points in space, Philos. Mag., 2, 559–572, 1901. 15911
Pilewskie, P. and Twomey, S.: Discrimination of ice from water in clouds by optical remote sensing, Atmos. Res., 21, 113–122, 1987. 15904
Rabbette, M. and Pilewskie, P.: Multivariate analysis of solar spectral irradiance measurements, J. Geophys. Res-Atmos., 106, 9685–9696, 2001. 15911
Sassen, K. and Wang, Z.: Classifying clouds around the globe with the CloudSat radar: 1-year of results, Geophys. Res. Lett., 35, L04805, doi:10.1029/2007GL032591, 2008. 15904
Shupe, M. D. and Intrieri, J. M.: Cloud radiative forcing of the Arctic surface: The influence of cloud properties, surface albedo, and solar zenith angle, J. Climate, 17, 616–628, 2004. 15903
Stachlewska, I., Wehrle, G., Stein, B., and Neuber, R.: Airborne Mobile Aerosol Lidar for measurements of Arctic aerosols, Proceedings of 22nd International Laser Radar Conference (ILRC2004), ESA SP-561, 1, 87–89, 2004. 15907
Stamnes, K., Tsay, S., Wiscombe, W., and Jayaweera, K.: A numerically stable algorithm for discrete-ordinate-method radiative transfer in multiple scattering and emitting layered media, Appl. Optics, 27, 2502–2509, 1988. 15909

Sun, Z. and Shine, K. P.: Studies of the Radiative Properties of Ice and Mixed-Phase Clouds, Q. J. Roy. Meteorol. Soc., 120, 111–137, 1994. 15903

Warren, S. G.: Optical-Constants Of Ice From The Ultraviolet To The Microwave, Appl. Opt., 23, 1206–1225, 1984. 15932

Wendisch, M. and Mayer, B.: Vertical distribution of spectral solar irradiance in the cloudless sky: A case study, Geophys. Res. Lett., 30, 1183, doi:10.1029/2002GL016529, 2003. 15905

Wendisch, M., Müller, D., Schell, D., and Heintzenberg, J.: An airborne spectral albedometer with active horizontal stabilization, J. Atmos. Oceanic Technol., 18, 1856–1866, 2001. 15906

Wendisch, M., Pilewskie, P., Jäkel, E., Schmidt, S., Pommier, J., Howard, S., Jonsson, H. H., Guan, H., Schroder, M., and Mayer, B.: Airborne measurements of areal spectral surface albedo over different sea and land surfaces, J. Geophys. Res.-Atmos., 109, D08203, doi:10.1029/2003JD004392, 2004. 15905

Wieliczka, D. M., Weng, S. S., and Querry, M. R.: Wedge Shaped Cell For Highly Absorbent Liquids – Infrared Optical-Constants Of Water, Appl. Optics, 28, 1714–1719, 1989. 15932

Yang, P. and Liou, K. N.: Finite-difference time domain method for light scattering by small ice crystals in three-dimensional space, J. Opt. Soc. Am. A., 13, 2072–2085, 1996. 15909

Yoshida, Y. and Asano, S.: Effects of the vertical profiles of cloud droplets and ice particles on the visible and near-infrared radiative properties of mixed-phase stratocumulus clouds, J. Meteor. Soc. Japan, 83, 471–480, 2005. 15903

ACPD

8, 15901–15939, 2008

Cloud phase identification of low-level Arctic clouds

A. Ehrlich et al.

Table 1. Ice indices I_S, I_P and I_A calculated for the observed clouds presented in Fig. 3a.

	liquid water	mixed	ice
I_S	8.8	29.8	57.0
I_P	0.6	5.5	12.1
I_A	*	1.17	1.37

Table 2. I_S, I_P and I_A of mixed-phase clouds (τ_W=13.5, τ_I=1.5) for different positions of the ice layer (not all 10 simulations shown here). The position is given by the optical depth τ_W^{top} of the liquid water layer above the single ice layer.

τ_W^{top}	I_S	I_P	I_A
0.0	42.0	7.8	1.08
1.5	32.8	6.0	1.01
3.0	26.1	4.8	1.00
6.0	16.4	3.4	1.00
9.0	13.5	2.5	1.00
13.5	11.9	1.6	1.00

ACPD
8, 15901–15939, 2008

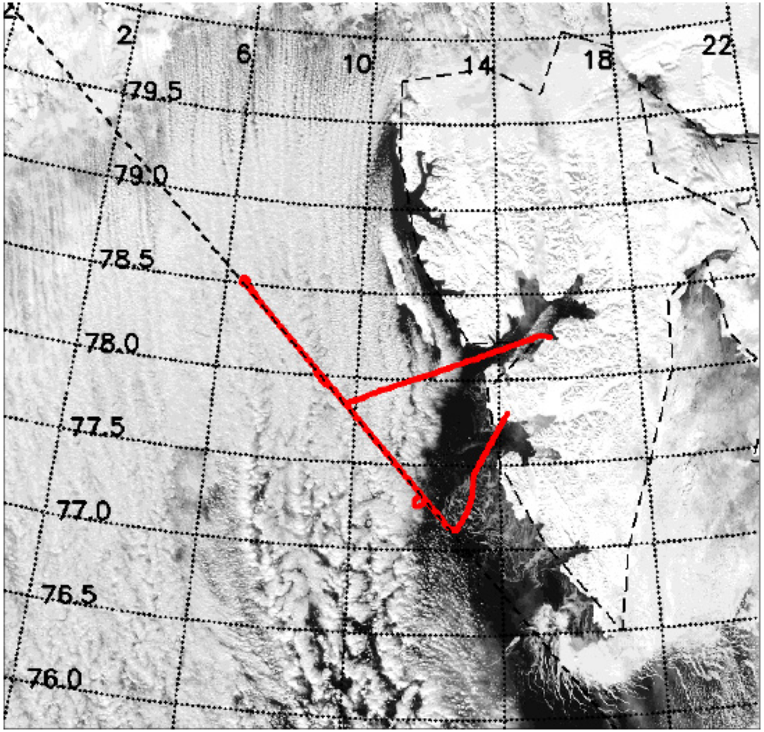

Fig. 1. MODIS satellite image of 7 April 2007 overlaid with the flight track of Polar 2 aircraft (red line) along the CALIPSO overpass (dashed black line). Numbers give the latitude and longitude, respectively.

ACPD

8, 15901–15939, 2008

Cloud phase identification of low-level Arctic clouds

A. Ehrlich et al.

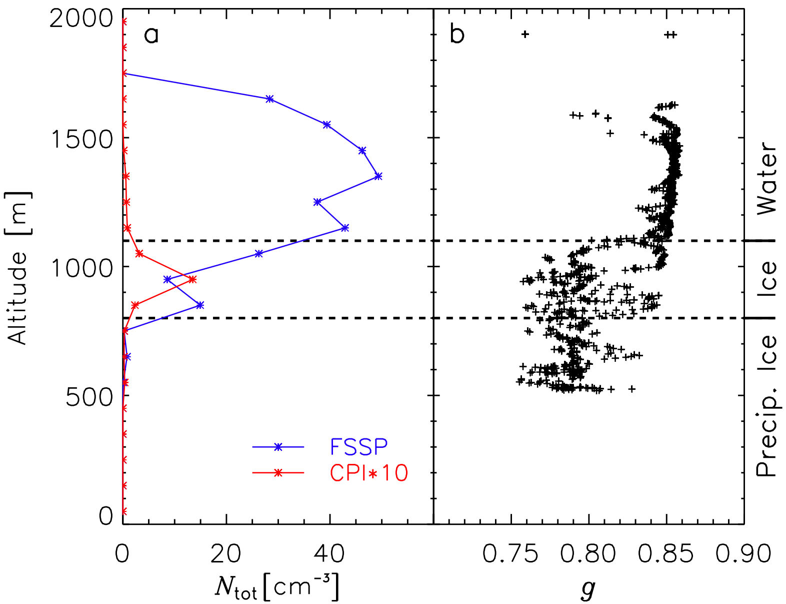

Fig. 2. Profile of microphysical measurements from 7 April 2007. Total particle concentration N_{tot} measured by FSSP and CPI are given in panel **(a)**. The asymmetry parameter g obtained from the Polar Nephelometer is shown in panel **(b)**.

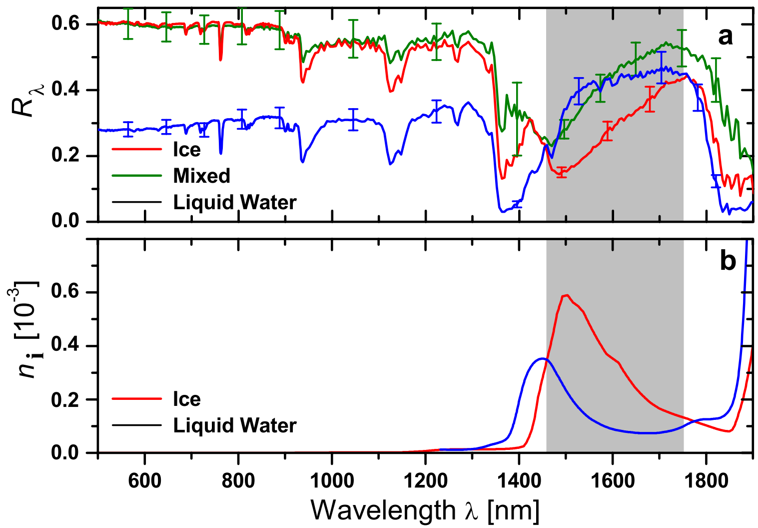

Fig. 3. Examples of measured cloud top reflectance R_λ (7 April 2007) over a pure ice cloud (τ=12), pure liquid water cloud (τ=4) and mixed-phase cloud (τ=15) are given in panel **(a)**. Panel **(b)** shows the imaginary part n_i of the refractive index for ice and liquid water.

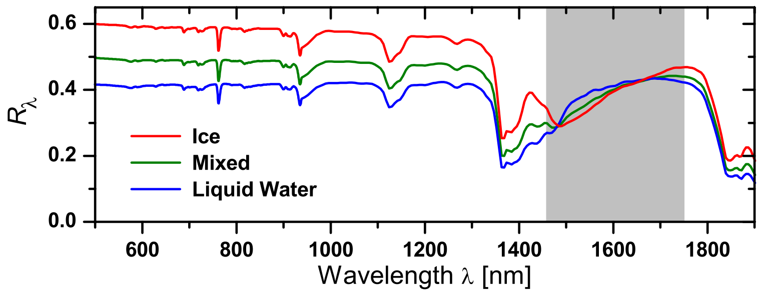

Fig. 4. Examples of simulations of cloud top reflectance R_λ for pure ice, pure liquid water and mixed-phase clouds with optical thickness of 12.

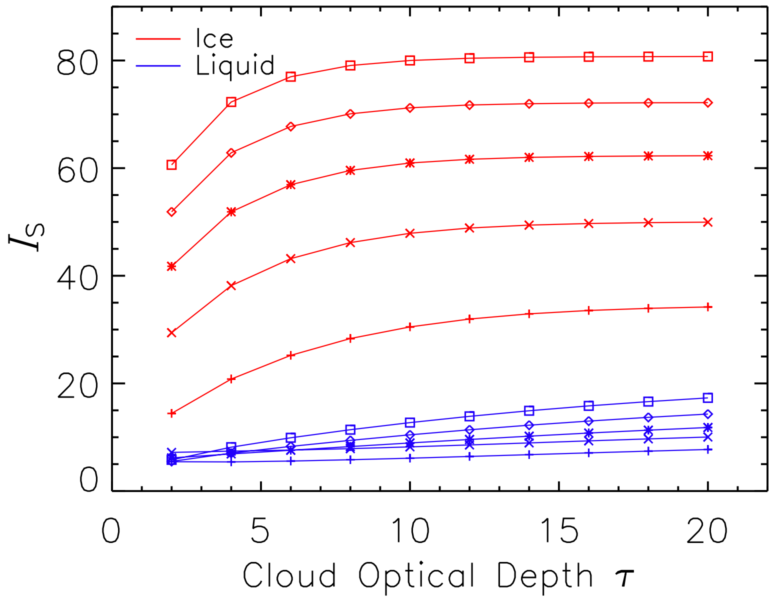

Fig. 5. Ice index I_S calculated from simulation of pure ice clouds (red) and pure liquid water clouds (blue). The different D_{eff} are marked by different symbols, plus (D_{eff}=30/8 μm), cross (D_{eff}=60/12 μm), star (D_{eff}=90/16 μm), diamond (D_{eff}=120/20 μm), square (D_{eff}=150/26 μm).

ACPD
8, 15901–15939, 2008

Title Page
Abstract Introduction
Conclusions References
Tables Figures
◂◂ ▸▸
◂ ▸
Back Close
Full Screen / Esc
Printer-friendly Version
Interactive Discussion

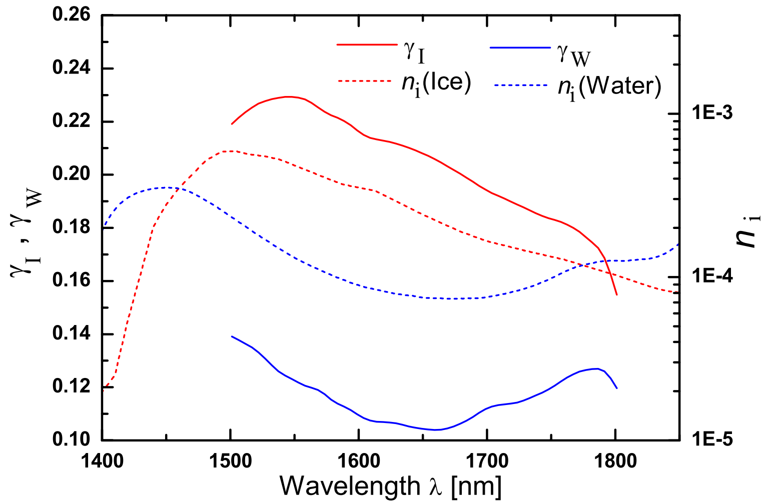

Fig. 6. Component weightings γ_I and γ_W for the calculation of the principle components PC_I and PC_W (solid lines). Dashed lines represent the imaginary part n_i of refractive index for ice and liquid water published by Warren (1984) and Wieliczka et al. (1989).

ACPD
8, 15901–15939, 2008

Title Page
Abstract
Introduction
Conclusions
References
Tables
Figures
◀|
|▶
◀
▶
Back
Close
Full Screen / Esc
Printer-friendly Version
Interactive Discussion

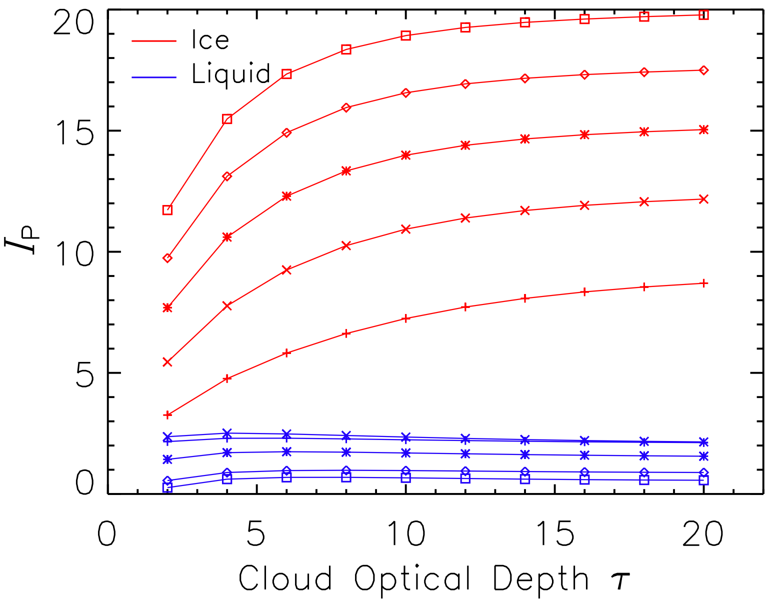

Fig. 7. Same as Fig. 5 for ice index I_P.

ACPD

8, 15901–15939, 2008

Cloud phase identification of low-level Arctic clouds

A. Ehrlich et al.

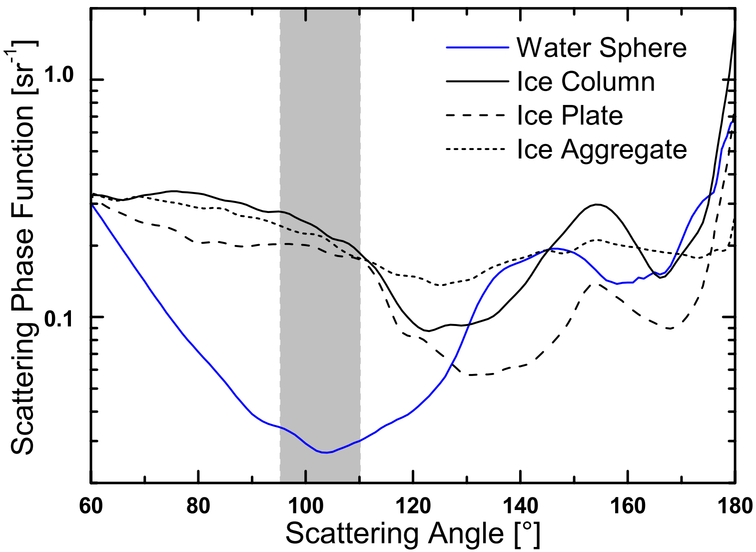

Fig. 8. Scattering phase function of different individual cloud particles at 640 nm wavelength. The diameter of the liquid water sphere is 16 μm. All ice crystals have a maximum dimension of 55 μm.

ACPD
8, 15901–15939, 2008

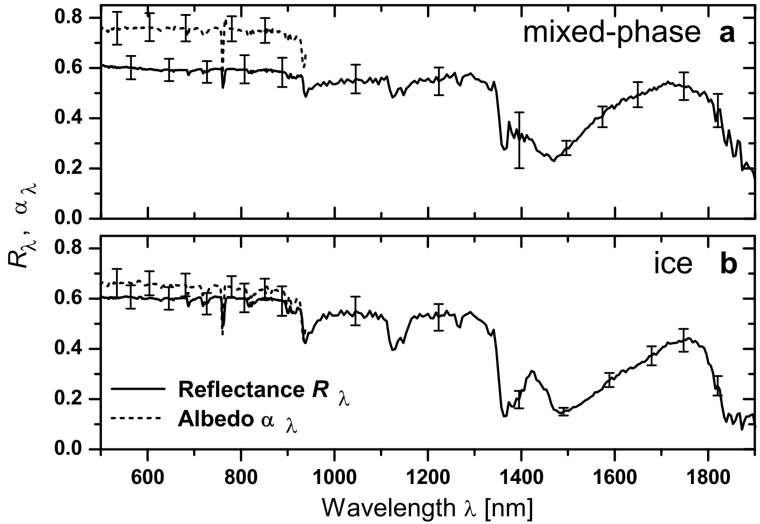

Fig. 9. Cloud top reflectance R_λ and cloud albedo α_λ measured on 7 April 2007 above a mixed-phase cloud **(a)** and a pure ice cloud **(b)**. The cloud optical thickness of both clouds was about 12.

ACPD
8, 15901–15939, 2008

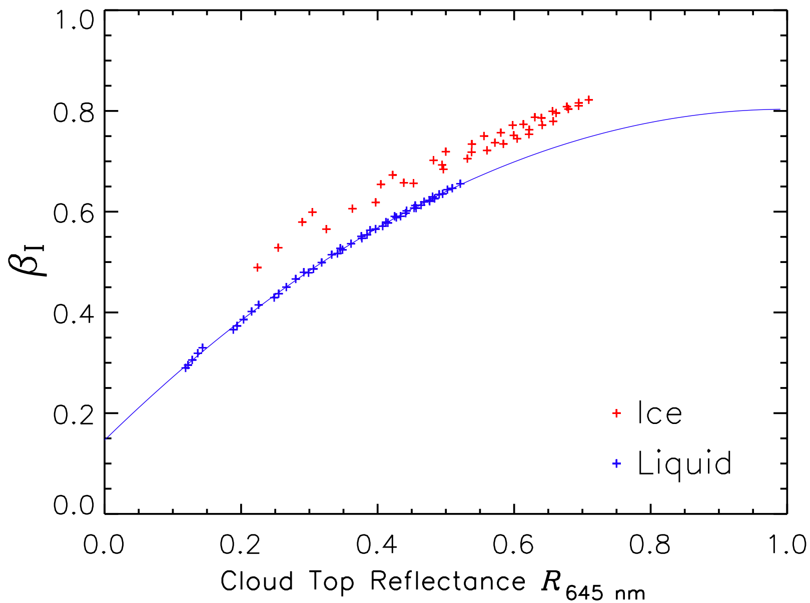

Fig. 10. Simulated β_I for pure liquid water clouds and pure ice clouds (column shaped crystals) of different optical thickness (τ=2–20) and effective diameter (8–26 μm for liquid water and 10–100 μm for ice clouds). The polynomial fit for the liquid water cloud is overlaid as solid line (β_I=0.15+1.32$\cdot R_\lambda$−0.67$\cdot R_\lambda^2$+0.01$\cdot R_\lambda^3$).

ACPD
8, 15901–15939, 2008

Title Page
Abstract | Introduction
Conclusions | References
Tables | Figures
◂| |▸
◂ ▸
Back | Close
Full Screen / Esc
Printer-friendly Version
Interactive Discussion

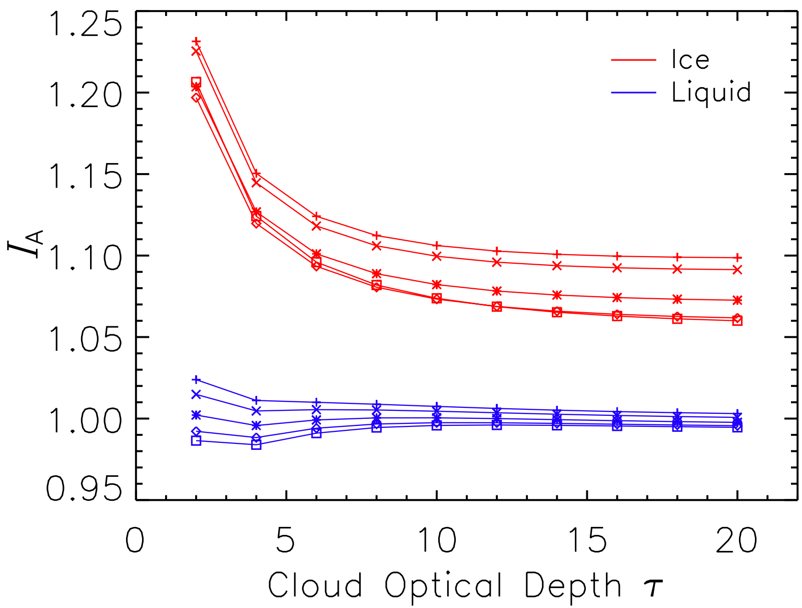

Fig. 11. Same as Fig. 5 for ice index I_A.

ACPD
8, 15901–15939, 2008

Title Page
Abstract | Introduction
Conclusions | References
Tables | Figures
◂◂ | ▸▸
◂ | ▸
Back | Close
Full Screen / Esc
Printer-friendly Version
Interactive Discussion

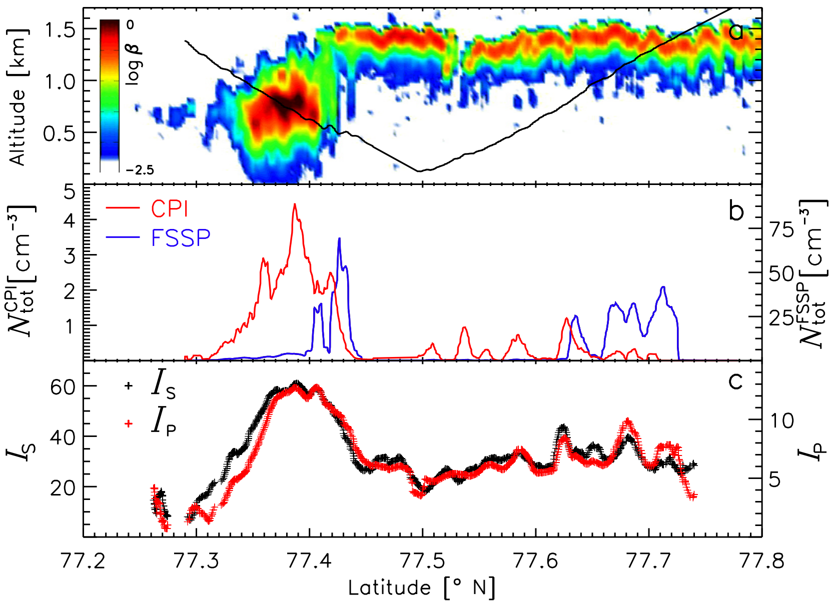

Fig. 12. Profile of total attenuated backscatter coefficient β [sr^{-1} km^{-1}] measured by CALIPSO in the cloud observed on 7 April 2007 **(a)**. The flight track of the in situ measurements is overlaid as black line. Ice and liquid water particle concentration N_{tot} measured by CPI and FSSP along the flight track and the ice indices I_S and I_P for the same positions are given in panels **(b)** and **(c)**.

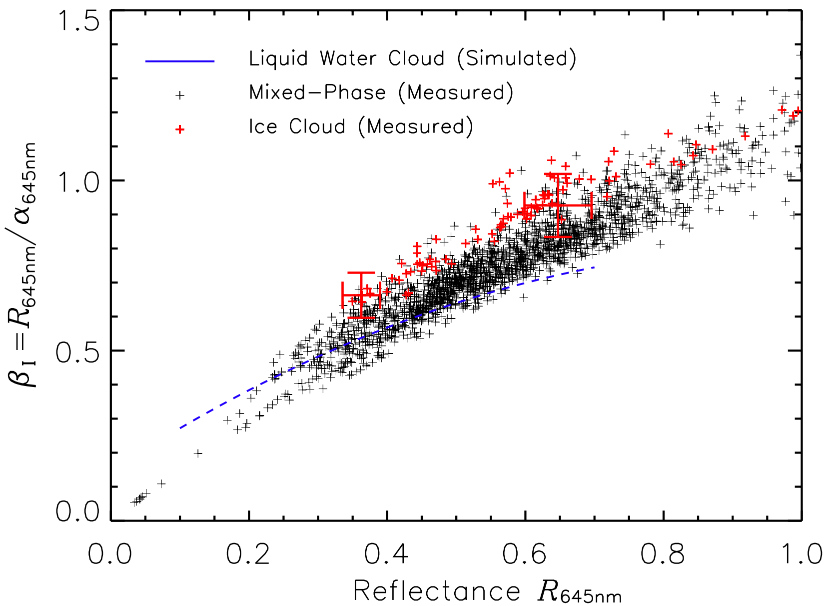

Fig. 13. Measured β_I as function of $R_{645\,nm}$. Black crosses show measurements over mixed-phase clouds, red crosses over the ice cloud observed on the cloud edge. Simulation for pure liquid water clouds are shown as blue line.

ACPD
8, 15901–15939, 2008

Cloud phase identification of low-level Arctic clouds

A. Ehrlich et al.